Composites: Part B 41 (2010) 462–474

Contents lists available at ScienceDirect

Composites: Part B

journal homepage: www.elsevier.com/locate/compositesb

Quasi-static and dynamic fracture of graphite/epoxy composites: An optical study of loading-rate effects

Dongyeon Lee [a], Hareesh Tippur [a,*], Phillip Bogert [b]

[a] Dept of Mechanical Engineering, Auburn University, Auburn, AL 36849, United States
[b] NASA Langley Research Center, Hampton, VA 44313, United States

ARTICLE INFO

Article history:
Received 12 January 2010
Received in revised form 9 April 2010
Accepted 14 May 2010
Available online 20 May 2010

Keywords:
A. Polymer-matrix Composites (PMCs)
B. Fracture
B. Impact behavior
D. Mechanical testing digital image correlation

ABSTRACT

Strain-rate effects on fracture behavior of unidirectional composite materials are studied. Single-edge notched multi-layered unidirectional graphite composites (T800/3900-2) are investigated to examine fracture responses under static and dynamic loading conditions using a digital speckle correlation method. The fracture parameters for growing cracks are extracted as a function of fiber orientation. A 2D digital image correlation (DIC) method is used to obtain time-resolved full-field in-plane surface displacements when specimens are subjected to quasi-static and impact loading. Stress intensity factor and crack extension histories for pure mode-I and mixed mode cases are extracted from the full-field displacements. When compared to the dynamic stress intensity factors at crack initiation, the static values are found to be consistently lower. The stress intensity factor histories exhibit a monotonic reduction under dynamic loading conditions whereas an increasing trend is seen after crack initiation under quasi-static loading cases. This is potentially due to dominant crack face fiber bridging effects in the latter cases.

1. Introduction

The stress–strain response of fiber-reinforced composites is susceptible to loading-rate effects. A few earlier investigations on fracture behavior of fiber reinforced plastics have indeed shown that to be the case [1–5]. However, these studies have focused on *interlaminar* fracture behaviors, which cannot be generalized for other fracture modes since interlaminar properties of such materials are generally different from the *intralaminar* properties.

A brief review of experimental studies on fracture mechanics of fiber-reinforced composites show that Tirosh [6], Donaldson [7], and Liu et al. [8] used global load and/or displacement measurements to study quasi-static fracture of composites. Among the crack tip field measurement approaches, Shukla et al. [9] developed strain-gage methods to evaluate stress intensity factors using one or two strain gages under quasi-static loading conditions. Later they extended the method to the measurement of dynamic stress intensity factors as well [10,11] using multiple gages. The strain-gage method provides good accuracy and convenience. However, being a point-wise measurement method, full-field information about deformations in the crack tip vicinity is unavailable. Full-field optical measurement methods, on the other hand, offer a number of advantages in the context of experimental fracture mechanics – they provide complete information on deformation components at various load levels, help locate the crack tip at various time instants, evaluate associated crack growth and fracture parameters, to name a few. The optical methods of caustics [12], photoelasticity [13], moiré interferometry [14], and thermoelastic fracture analysis [15] are among the successfully used full-field methods to study of dynamic fracture of isotropic and anisotropic [16] materials. Another more recent full-field measurement technique is a lateral shearing interferometer called Coherent Gradient Sensing (CGS) [17,18]. Rosakis and coworkers have reported a few studies on dynamic fracture behavior of unidirectional composite laminates using this technique [19–21]. These optical methods, however, require extensive specimen surface preparation. In recent years, the digital image correlation (DIC) technique has become a relatively popular [22–28] tool as surface preparation requirements are not as elaborate as in case of interferometric methods.

Although DIC methods have been in practice for over two decades, applications to fracture mechanics problems in general and dynamic fracture in particular have been relatively few [29–32]. The early work of McNeill et al. [22] demonstrated DIC for extracting quasi-static mode-I stress intensity factors using crack opening displacements. Measurement of crack tip opening angles (CTOA) using DIC was used by Dawicke and Sutton [29] to investigate slow elasto-plastic tearing of aluminum sheets. A mixed-mode quasi-static fracture study using the DIC method has been reported by Yoneyama et al. [30]. DIC was extended by Abanto-Bueno and

* Corresponding author. Tel.: +1 334 844 3327.
E-mail address: htippur@eng.auburn.edu (H. Tippur).

1359-8368/$ - see front matter © 2010 Elsevier Ltd. All rights reserved.
doi:10.1016/j.compositesb.2010.05.007

Lambros [31] to the study quasi-static mixed-mode crack growth in nonhomogeneous, isotropic inelastic polymer sheets with graded mechanical properties. Rethore et al. [32] have used DIC in conjunction with path independent interaction integrals to accurately evaluate mixed-mode stress intensity factors near cracks. The disadvantages of dealing with noisy displacement gradients while evaluating stress intensity factors using domain integrals have been overcome by Rethore et al. [33] by coupling DIC with the virtual crack extension approach. The feasibility of performing a quasi-static SIF extraction in cracked orthotropic composites is reported by Mogadpalli and Parameswaran [34] using DIC.

Even though aforementioned investigations have shown the feasibility of DIC to study fracture problems, most have been carried out under quasi-static conditions. The challenges of implementing DIC under stress-wave dominant conditions with crack speeds reaching several hundreds of meters per second and fracture events lasting only a few hundred microseconds are substantial. These obstacles have been overcome recently by Kirugulige et al. [35] and Kirugulige and Tippur [36] using DIC in conjunction with a digital ultra high-speed camera. In these efforts, mode-I and mixed-mode dynamic fracture behaviors of brittle isotropic materials were studied. The extension of DIC to the study of dynamic fracture of fiber-reinforced composites offers additional challenges. Due to a relatively high material stiffness and the presence of fiber–matrix interfaces, crack speeds in unidirectional composites are substantially higher and the magnitude of displacements in the crack vicinity is smaller relative to comparable isotropic materials. A recent work by Lee and Tippur [37] has demonstrated the feasibility of DIC to study fracture of composite materials.

In this work, the previously developed DIC methodology coupled with high-speed photography is used to study loading-rate effects on fracture behavior of unidirectional graphite/epoxy composite laminates. The mixed-mode (mode-I + mode-II) fracture responses and parameters obtained from quasi-static and impact loading experiments are comparatively examined for various fiber orientations relative to the loading direction. The optical measurements and the subsequent analyses are carried out within the framework of continuum based linear elastic fracture mechanics theories. That is, the composite material in question is treated as a macroscopically homogeneous, orthotropic elastic medium and no particular attention is given to microscopic material inhomogeneities while extracting fracture parameters.

In the following, displacement fields near the vicinity of a crack tip in an orthotropic medium are first reviewed. The DIC approach and experimental setup employed in static and dynamic experiments are described next. Subsequently, the displacement field results and crack growth behaviors in quasi-static and dynamic experiments are presented. Following a discussion of dynamic effects and linear versus nonlinear least-squares analysis displacements to extract of stress intensity factors, fracture toughness histories for different fiber orientations is presented. Quasi-static and dynamic fracture toughness as a function of material anisotropy parameters is reported and relevant conclusions are offered.

2. Crack-tip displacement fields

In order to extract the mode-I and -II stress intensity factors from full-field measurements, a continuum mechanics based description of the respective field quantities is used. In this work, 2D DIC is used to measure in-plane Cartesian displacement fields in the vicinity of stationary and growing cracks. These displacement components u_x and u_y for a mixed-mode crack are expressed as follows [38]:

$$\begin{aligned} u_x &= K_{\mathrm{I}}\sqrt{\frac{2r}{\pi}}\mathrm{Re}\left[\frac{1}{\mu_2-\mu_1}(p_1\mu_2 z_1 - p_2\mu_1 z_2)\right] \\ &\quad + K_{\mathrm{II}}\sqrt{\frac{2r}{\pi}}\mathrm{Re}\left[\frac{1}{\mu_2-\mu_1}(p_1 z_1 - p_2 z_2)\right] + \ldots \\ u_y &= K_{\mathrm{I}}\sqrt{\frac{2r}{\pi}}\mathrm{Re}\left[\frac{1}{\mu_2-\mu_1}(q_1\mu_2 z_1 - q_2\mu_1 z_2)\right] \\ &\quad + K_{\mathrm{II}}\sqrt{\frac{2r}{\pi}}\mathrm{Re}\left[\frac{1}{\mu_2-\mu_1}(q_1 z_1 - q_2 z_2)\right] + \ldots \end{aligned} \tag{1}$$

where quantities p_j, q_j, and z_j are defined as

$$p_j = \mu_j^2 s_{11} + s_{12} - \mu_j s_{16}$$

$$q_j = \mu_j s_{12} + \frac{s_{22}}{\mu_j} - s_{26}$$

$$z_j = \sqrt{\cos\theta + \mu_j \sin\theta}$$

μ_j ($j = 1, 2$) are the two roots with positive imaginary part of the equation

$$s_{11}\mu^4 - 2s_{16}\mu^3 + (2s_{12} + s_{66})\mu^2 - 2s_{26}\mu + s_{22} = 0 \tag{2}$$

where s_{ij} are the elements of compliance matrix such that

$$\begin{bmatrix} \varepsilon_{xx} \\ \varepsilon_{yy} \\ \varepsilon_{zz} \\ \gamma_{yz} \\ \gamma_{zx} \\ \gamma_{xy} \end{bmatrix} = \begin{bmatrix} s_{11} & s_{12} & s_{13} & s_{14} & s_{15} & s_{16} \\ s_{21} & s_{22} & s_{23} & s_{24} & s_{25} & s_{26} \\ s_{31} & s_{32} & s_{33} & s_{34} & s_{35} & s_{36} \\ s_{41} & s_{42} & s_{43} & s_{44} & s_{45} & s_{46} \\ s_{51} & s_{52} & s_{53} & s_{54} & s_{55} & s_{56} \\ s_{61} & s_{62} & s_{63} & s_{64} & s_{65} & s_{66} \end{bmatrix} \begin{bmatrix} \sigma_{xx} \\ \sigma_{yy} \\ \sigma_{zz} \\ \tau_{yz} \\ \tau_{zx} \\ \tau_{xy} \end{bmatrix} \tag{3}$$

The coordinates x and y are the two principal directions of a composite sample as illustrated in Fig. 1 with r the radial distance from the crack tip, θ the angle relative to the x-axis, and β the fiber orientation angle. It should also be noted that Eq. (1) can be used for situations before crack initiation in impact loading situations when inertia effects are dominant. In doing so, it is implicitly assumed that inertial effects enter stress intensity factors K_{I} and K_{II}.

Eq. (1) can be extended to impact loading conditions where transient effects associated with crack-tip velocity are present. For such cases displacement fields u_x and u_y are given in Ref. [8] and are derived from Stroh's formulation [39] as

$$\begin{aligned} u_x &= \frac{1}{c_{66}R(v)}\sqrt{\frac{2r}{\pi}}\mathrm{Re}\left[\left(\frac{\mu_2^d-\lambda_2}{\lambda_1-\lambda_2}z_1 - \frac{\mu_1^d-\lambda_1}{\lambda_1-\lambda_2}z_2\right)K_{\mathrm{ID}}\right. \\ &\quad \left. -\left(\frac{\gamma-\lambda\eta^2\mu_2^d\lambda_2}{\lambda_1-\lambda_2}z_1 - \frac{\gamma-\lambda\eta^2\mu_1^d\lambda_1}{\lambda_1-\lambda_2}z_2\right)K_{\mathrm{IID}}\right] \\ u_y &= \frac{1}{c_{66}R(v)}\sqrt{\frac{2r}{\pi}}\mathrm{Re}\left[-\left(\lambda_1\frac{\mu_2^d-\lambda_2}{\lambda_1-\lambda_2}z_1 - \lambda_2\frac{\mu_1^d-\lambda_1}{\lambda_1-\lambda_2}z_2\right)K_{\mathrm{ID}}\right. \\ &\quad \left. +\left(\lambda_1\frac{\gamma-\lambda\eta^2\mu_2^d\lambda_2}{\lambda_1-\lambda_2}z_1 - \lambda_2\frac{\gamma-\lambda\eta^2\mu_1^d\lambda_1}{\lambda_1-\lambda_2}z_2\right)K_{\mathrm{IID}}\right] \end{aligned} \tag{4}$$

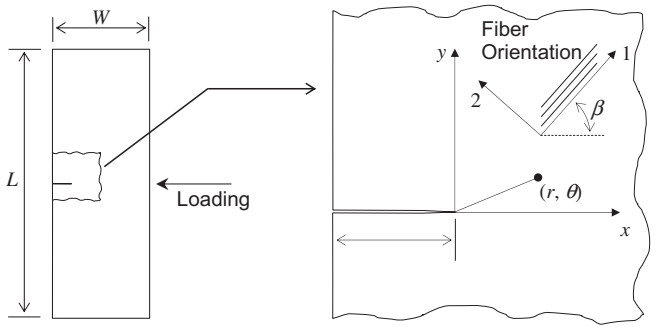

Fig. 1. Illustration of crack-tip neighbourhood (L = 200 mm, W = 50 mm, a = 0.2W).

where μ_j^d ($j = 1, 2$) are the two roots with positive imaginary part of the equation

$$\mu^4 + \left(\alpha_l^2\eta^2 + \frac{\alpha_s^2}{\eta^2\lambda} - \frac{(1+\gamma)^2}{\eta^2\lambda}\right)\mu^2 + \frac{\alpha_l^2\alpha_s^2}{\lambda} = 0 \tag{5}$$

and K_{ID} and K_{IID} are dynamic stress intensity factors for mode-I and mode-II, respectively. These expressions are valid for an orthotropic body in which crack-tip velocity is in the subsonic regime. That is, crack-tip velocity is lower than the shear wave speed.

The other parameters in Eq. (4) are defined as follows [8]:

$$\lambda = \frac{s_{11}}{s_{22}}, \quad \rho = \frac{2s_{12}+s_{66}}{2\sqrt{s_{11}s_{22}}}, \quad \kappa = \frac{3\sqrt{s_{11}s_{22}}+s_{12}}{\sqrt{s_{11}s_{22}}-s_{12}},$$
$$c_l = \sqrt{\frac{c_{11}}{d}}, \quad c_s = \sqrt{\frac{c_{66}}{d}}, \quad \alpha_l^2 = 1 - \left(\frac{v}{c_l}\right)^2,$$
$$\alpha_s^2 = 1 - \left(\frac{v}{c_s}\right)^2, \quad \eta^2 = \left(\frac{\kappa+1}{\kappa-1}\right)\left(\frac{3-\kappa+\rho(\kappa+1)}{4\sqrt{\lambda}}\right),$$
$$\gamma = \sqrt{\lambda}\eta^2\frac{3-\kappa}{1+\kappa}, \quad \lambda_j = \frac{\eta^2\alpha_l^2+\mu_j^2}{(1+\gamma)\mu_j} \ (j = 1, 2),$$
$$R(v) = \sqrt{\lambda}\eta^2\alpha_l\alpha_s - \frac{\sqrt{\lambda}\eta^2\alpha_l + \gamma^2\alpha_s}{\sqrt{\lambda}\eta^2\alpha_l + \alpha_s} \tag{6}$$

in which $c_{ij}(i, j = 1, \ldots, 6)$ are the elements of stiffness matrix, c_l the longitudinal wave speed, c_s the shear wave speed, v the crack-tip velocity, and d the mass density. Note that rho (ρ) here is not the conventional notation of mass density. According to Liu et al. [8], the condition $\alpha_l\alpha_s > 0$ must be met for the expressions to be valid. Therefore, the sign of α_l should be equal to that of α_s.

It is worth noting that crack tip fields at finite distances away from the tip are typically affected by higher order terms as demonstrated by Xia et al. [40] for the case of crack propagation along a distinct interface within a specimen. In this work, estimation procedure includes only the dominant terms of the asymptotic expansion with an implicit assumption that by selecting data close to the crack tip, the influence of higher order terms can be minimized although not entirely eliminated.

3. Experimental details

3.1. Optical method

The basic idea of the 2D DIC technique in the context of fracture mechanics is to monitor decorated random speckles (or natural texture) on a specimen surface during a fracture event in order to quantify displacements. Photographed light intensity (gray scale) of speckle patterns before and after deformation are correlated for extracting 2D planar displacement components. In this work, digitized light intensity data are analyzed using in-house software on a MATLAB™ platform. A three-step approach, described in Refs. [35,36], was employed for measuring displacements at discrete locations of a rectangular grid around the crack tip. First, an initial estimation of displacements was made. A two-dimensional cross-correlation between the two selected sub-images was carried out in the Fourier domain. The peak of the correlation function was detected to an accuracy of 1/16 of a pixel using bicubic interpolation. As described in Chen et al. [41], displacement fields u and v were obtained using a cross-correlation exponent $\alpha = 0.25$.[1] In the next step, in order to refine displacement fields obtained previously, a spatial domain iterative approach was used to minimize the 2D correlation coefficient by using a nonlinear least-squares minimization technique. Minimization was carried out in a six-variable space (*viz.*, u and v as well as their four gradient components; $\partial u/\partial x$, $\partial u/\partial y$, $\partial v/\partial x$, $\partial v/\partial y$) by using values that were obtained previously. In this step, a significant amount of noise present in the earlier estimation was removed from the u and v fields. Lastly, crack-tip displacements were smoothed using an algorithm applied to (u, v) displacement fields separately. While smoothing, the displacements were kept discontinuous across the two crack faces since upper and lower halves undergo different deformations. The data corresponding to the crack faces were excluded from the smoothing operation to preserve displacement discontinuity across the crack faces. The smoothing method in the current work employed an unbiased optimum smoothing parameter based on the noise level present in the displacement field. The details of the regularization technique and smoothing can be found in Refs. [42,43], respectively, and are avoided here for brevity.

Here it should be noted that although step-2 provides a reasonably accurate estimate of displacements (and hence the fracture parameters, to be discussed later on), the data contains noise due to the choice of the sub-image size, number of overlapping pixels of neighboring sub-images, accuracy of the minimization scheme used, etc., during image correlation. Accordingly, for a better interpretation of the resulting displacement fields, additional smoothing (step-3) is desirable. Furthermore, the interpretation of the data based on continuum concepts also demands this additional step. Apart from significant aesthetic improvements to the displacement field after this final step, step-3 is essential for strain field evaluation because strains obtained directly from displacements estimated after step-2 are prohibitively noisy. This will be addressed in more detail in Section 5.

3.2. Sample preparation

Unidirectional composite panels were fabricated from 35 plies of T800/3900-2 (supplied by Toray Composites America, Inc.) prepreg tapes formed by hot-compression molding. Rectangular coupons were then cut from the panels with four different fiber orientations relative to a short side of the specimen; 0°, 15°, 30°, and 45°. At this stage a coupon was slightly larger than the target size of $200 \times 50\ mm^2$. After coupons were polished along the edges, a 10-mm long pre-notch was made on each coupon using a 300 μm thick circular diamond impregnated saw. The crack tip was further sharpened by pressing a razor blade into it. The relative angle between the fibers and pre-notch direction determines the angle β.

Elastic constants for the given material are listed in Table 1. The subscripts 1 and 2 represent longitudinal and transverse directions relative to the fiber orientation, respectively (see Fig. 1). Although L–T notation is more common to describe direction vectors, the numeral system is adopted here in order to utilize the xyz coordinate system as well. For other configurations, moduli and Poisson's

Table 1
Material properties of T800/3900-2 composite.

	$\beta = 0°$[a]	$\beta = 15°$[b]	$\beta = 30°$[b]	$\beta = 45°$[b]
Modulus[c]				
E_{xx}	171.60	64.77	24.80	14.08
E_{yy}	8.25	8.67	10.20	14.08
G_{xy}	6.21	6.51	7.22	7.63
Poisson's ratio				
v_{xy}	0.344	0.252	0.190	0.134

[a] In-house measurement.
[b] By computation.
[c] E and G in GPa.

[1] The constant α in cross-correlation operator can be any number between 0 and 1 depending upon the quality of the impulse function. After a systematic study, it was found that the constant more than 0.5 often generated spurious result, and a lower value was needed to suppress high-peak noises.

ratios were computed by rotational transformation and are shown in Table 1.

The pre-notched fracture specimens were then sprayed with black and white paints successively to create a random speckle pattern. The resulting speckles were optimally sized by trial and error for obtaining the desired resolution. In this work, the typical speckle size was such that it covered 4–6 pixels of the imaging array of the camera. The mean value of the recorded grayscale ranged between 100 and 120 on a 0–255 scale. The histogram of the recorded grayscale was also optimized to have an approximate Gaussian distribution as shown in Fig. 2.

3.3. Testing procedure

3.3.1. Quasi-static fracture tests

Static experimental setup, shown schematically in Fig. 3, consisted of an Instron-4465 load frame (indicated by 1), a Nikon D100 digital camera (2), two white-light sources (3), and two data acquisition computers (4 and 5). The fracture specimen (6) was rested on a three-point bending platform and displacement controlled loading was applied at a cross-head speed of 0.004 mm/s. Since the time duration of the entire fracture event was relatively large (and the crack-tip velocity was slow even after crack initiation),

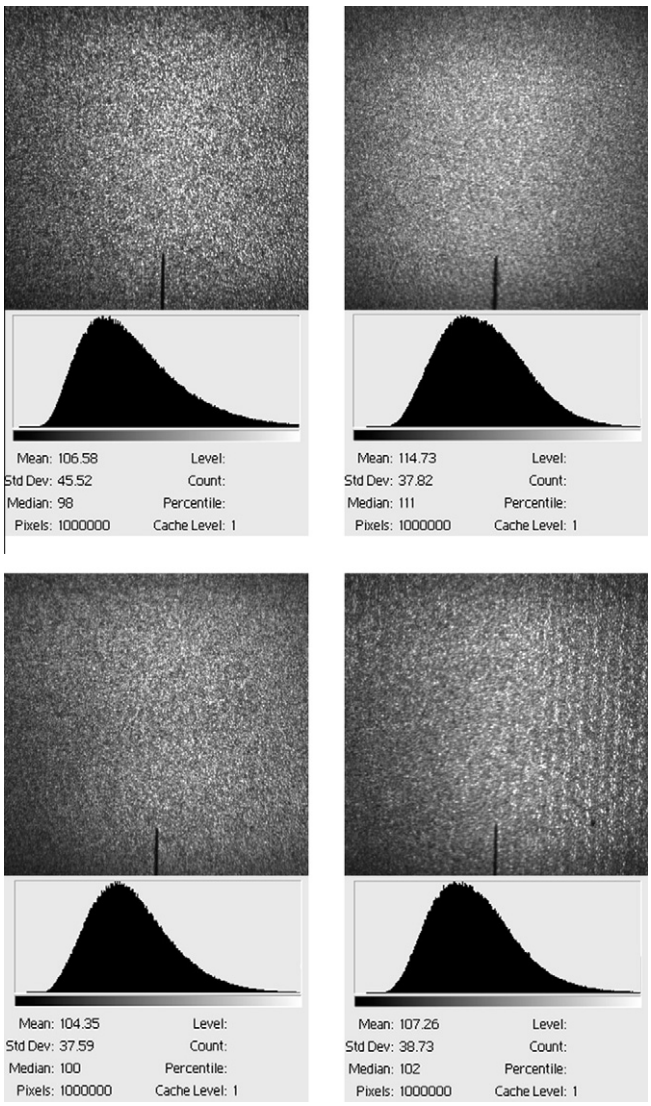

Fig. 2. Selected speckle images and histograms of the corresponding near-Gaussian grayscale distributions.

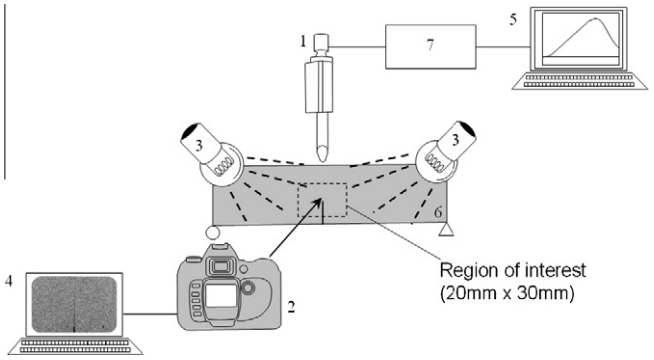

Fig. 3. Schematic of the experimental setup used for static tests: (1) cylindrical loading tip of the crosshead, (2) digital camera, (3) white-light sources, (4) DAQ 1, (5) DAQ 2, (6) specimen, (7) load cell.

images were photographed at a slow framing rate of 0.5 frames/s. Each 8-bit image was set to contain 1500 × 1000 pixels.

As soon as the sample began experiencing the load, time-lapse photography was initiated. The load *vs.* deflection data was acquired by one of the computers while the other recorded images captured by the camera. The file names for images were time-tagged by default, and were used later on to synchronize images with the corresponding applied load. The recording was continued until the crack initiated and propagated to the upper region of interest monitored by the camera. The time duration for the total fracture event ranged from 90 to 130 s depending upon the fiber orientation angle of the specimen.

In quasi-static three-point bending tests, a small load (about 10 N) was needed to overcome excessive rigid body motion due to any slack in loading fixtures. In the present work, images at approximately 30 N of load were used as reference (zero load) images for image correlation operations. The resulting error due to this approximation was relatively small due to the fact that failure in specimens occurred typically in the range of 600–1400 N.

3.3.2. Dynamic fracture tests

The dynamic experimental setup, shown schematically in Fig. 4, consisted of an Instron-Dynatup 9250-HV drop tower delivering impact loads and a Cordin 550 high-speed digital camera (indicated by 1) for recording images in real time during a fracture event. The drop tower had an instrumented impactor head (2) for recording the impact force history and a pair of anvils for recording support reaction histories. The setup also consisted of a delay generator (3; Model 555 by Berkeley Nucleonics Corp.) to generate a trigger pulse when the impactor head contacted the specimen (4). Since all the images were recorded during the dynamic event lasting less than 200 μs, the setup employed two high-intensity flash lamps (5; Cordin Model 659), triggered by the camera, to illuminate the specimen surface. As in the quasi-static tests, two separate computers were used; one (6) for recording impact force and anvil reaction histories and the other (7) for controlling the high-speed camera and storing photographed images.

A detailed experimental procedure for recording dynamic events can be found in a previous publication [37] and hence only a brief description is presented here. Prior to impacting the specimen, a set of 32 images of the specimen was photographed at a desired framing rate (250,000 frames per second in the current work). At this stage, the camera and flash lamps were initiated by an external trigger. While keeping all experimental parameters the same, a second set of 32 images were photographed as the specimen was subjected to transient loading. The camera and flash lamps were triggered when the impactor head contacted the top edge of the specimen. For every image in the deformed image set, there was a corresponding image in the undeformed image

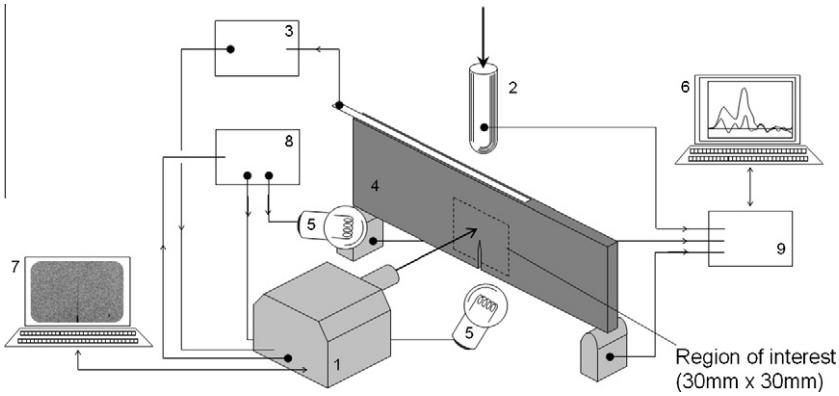

Fig. 4. Schematic of the dynamic experimental setup: (1) high-speed digital camera, (2) impactor tup of the drop tower, (3) delay generator, (4) specimen, (5) light sources, (6) DAQ 1, (7) DAQ 2, (8) lamp control unit, (9) drop-tower controller.

set obtained by the same CCD sensor array/optical relay circuit. After identifying the first image photographed for undeformed and deformed image sets, pairing the two images from each set was done. Each pair of these 32 matched images was analyzed subsequently. In this work, the impact velocity was 4.8 m/s.

The sub-image size used was 26×26 pixel^2, without any overlap between sub-images. After correlation of a sub-image was performed, the next sub-image of undeformed and deformed images was selected so that no uncorrelated area was present. In this study, due to zero overlap between pixels, resulting array size was 37×37 for images recorded using the high-speed camera.

4. Test results

4.1. Quasi-static test

A sequential arrangement of selected images during a static test on specimens with fiber orientation angle β of 45° is shown in Fig. 5. The crack tip location is shown by an arrow along the fiber direction. Unlike neat epoxy in which the crack rapidly accelerates to a speed of several hundred meters per second even for quasi-static loading (and hence capturing the crack initiation is not feasible with slow speed time-lapse photography), in graphite/epoxy the crack propagation speed is relatively low. This is primarily due to crack faces bridged by the fibers of the composites.

The MATLAB code was used to generate a 32×49 array of in-plane displacement components over the entire area for each image. These were evaluated using correlation of neighboring sub-images with a zero overlap among pixels. Using such arrays for every loading step, the in-plane displacement contour plots were obtained. The corresponding crack sliding displacement, u_x, and opening displacement, u_y, for the photographed images are also shown in Fig. 5. The increment used to depict displacements in these plots is 2 μm per contour (the smallest measureable displacement for the parameters used in this study is ~1.6 μm). These estimated displacement values along with the aid of Eq. (1) were subsequently used to extract stress intensity factors.

For all the selected angles, the crack length is plotted against time in Fig. 6. It must be noted that time "0" corresponds to the time instant when loading begins. Although the crack-tip velocities are quite low for quasi-static loading cases, it is notable that (initial) slopes of the curves in Fig. 6 decrease significantly from smaller fiber orientation angle to the larger ones.

4.2. Dynamic test

A few selected speckle images and the corresponding displacement fields are shown in Fig. 7 from dynamic experiments. For the same fiber orientation angle, the displacement fields in the dynamic cases show differences when compared to the quasi-static counterparts. For instance, immediately after crack initiation, contour lines of u_y at $t = 92$ μs in Fig. 7 are disturbed by a second set of isolines approaching from the right-hand side of the window of observation (as opposed to those at, say, $t = 91$ s in Fig. 5). This is due to impact loading occurring at the opposite edge of the specimen. This also requires that the stress intensity factor estimation process, in situations where the crack tip is close to the impact edge, should consider higher order terms in the analysis.

The crack length histories are plotted in Fig. 8. As in quasi-static cases, the initial slopes for each fiber orientation angle β are clearly distinguishable from one another. The best estimates of initial slope are 510, 370, 310, 220 m/s, for increasing angles of 0°, 15°, 30° and 45°, respectively. The crack-tip velocity is then computed based on information of the crack length against time. Before computing velocity, the data sets were smoothed using cubic Bezier curves and velocity was evaluated at the mid-point of each interval. The smoothed values were used to extract crack-velocity with the central difference method. The results thus obtained for each fiber orientation angle are shown in Fig. 9.

The maximum velocity attained by the crack in these four cases is approximately 560, 510, 460, and 520 m/s, respectively. (These values are only the best estimates due to the finite time intervals of 4 μs between images and smoothing of crack length history both of which tends to lower the values.) It is interesting to note in Fig. 9 that as the fiber orientation angle increases, the crack initiation is delayed and the peak velocity is attained earlier for $\beta = 0°$, and progressively later for 15°, 30°, and 45° cases. These will be further discussed later in terms of stress intensity factor histories.

5. Discussion

5.1. General considerations

The displacement data used in the analysis was limited to the region $0.5 < r/B < 1.5$ and $-135° < \theta < 135°$ (B is the sheet thickness and 0° is along the pre-notch direction) to avoid any potential 3D effects. Radial displacement field, u_r, was selected for estimating stress intensity factors due the robustness of the method established after comparison of stress intensity factor results with those from a complementary finite element analysis [37].

As demonstrated in Ref. [36], the pure mode-I stress intensity factors evaluated by taking into account the transient effects associated with the crack-tip velocity (for velocities lower than ~50% of the shear wave speed) are relatively small when compared to those evaluated using Eq. (1). To ensure that this is also true for mixed-

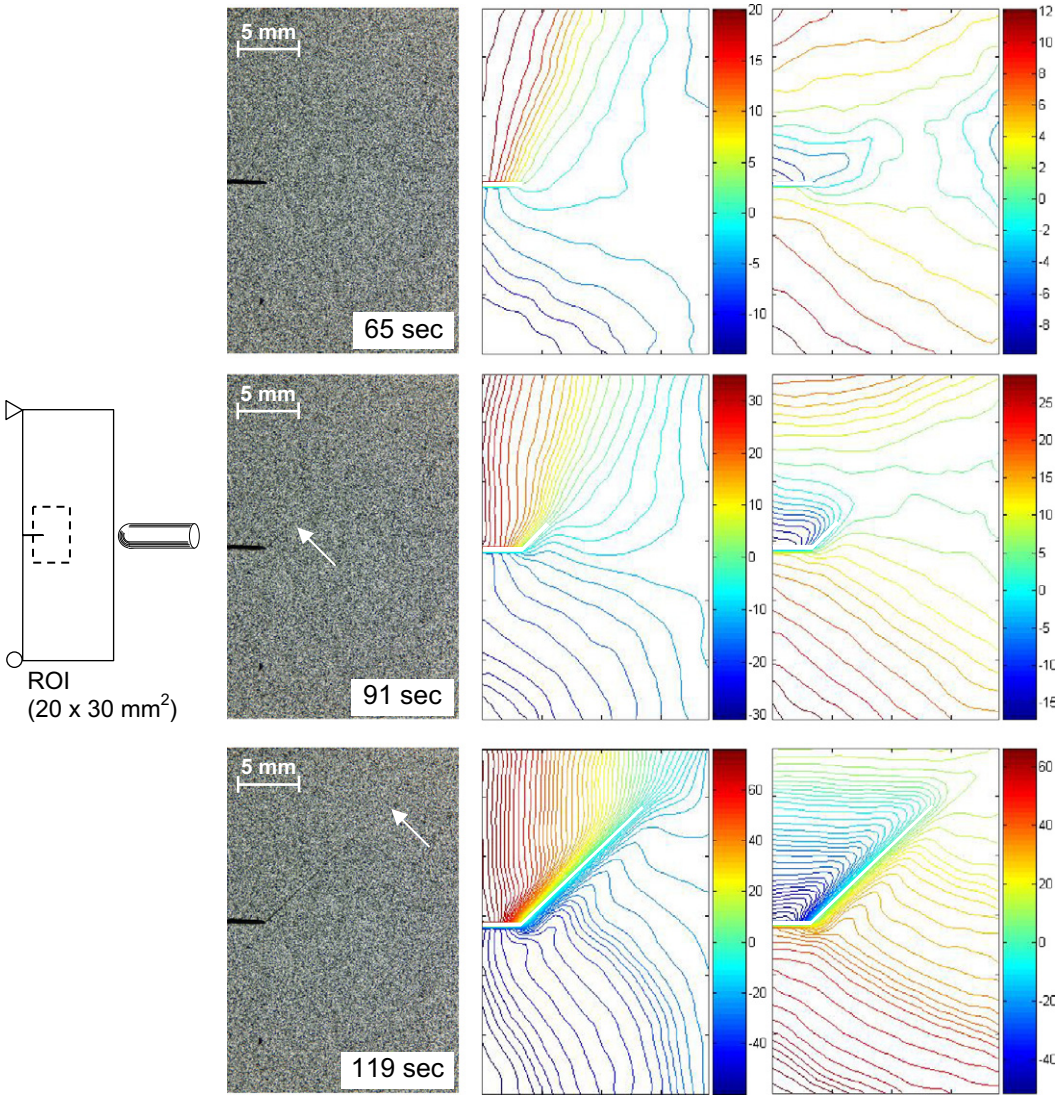

Fig. 5. Representative speckle images for static case ($\beta = 45°$; 20×30 mm^2) with full-field opening (second column) and sliding (third column) displacement contours (crack initiation takes place at $t \sim 77$ s): Moving crack tip is indicated by an arrow and the dark line is the initial crack in photographed images. Tick interval in the axes of displacement fields is 5 mm. Color-bar indicates displacement in micrometers. Contour interval is 2 μm.

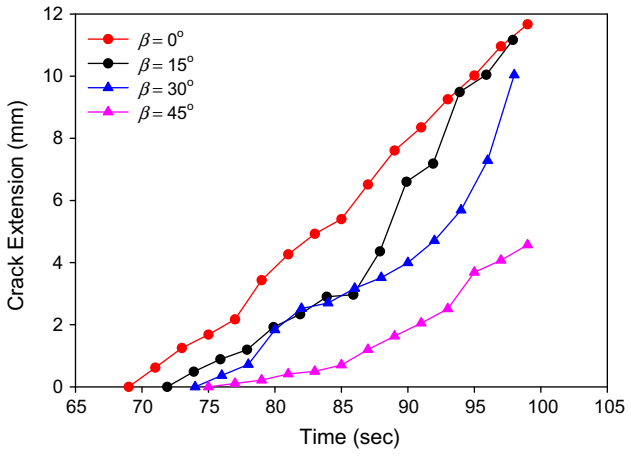

Fig. 6. Crack growth histories for static loading cases. Initial slopes are approximately estimated 0.41, 0.25, 0.27, 0.12 (mm/s) for $\beta = 0°$, 15°, 30°, 45°, respectively.

mode conditions, the stress intensity factors were computed with the aid of Eq. (4) and the results are shown in Fig. 10. In all cases, the deviation from those computed from Eq. (1) is negligible. In fact, the error margin in K_I is up to 6% for 0° case, and it progressively reduces down to 3% for higher fiber orientation angles. This suggests that transient effects associated with the crack-tip velocity are more evident in the 0° case for which velocity is the highest whereas the effects are negligible for higher-angles. The difference in mode-II stress intensity factor K_{II} (the smaller of the two stress intensity factors) was about 10%.

The moving crack tip was identified with the aid of real-time speckle images as well as the discontinuity in displacement contours. The crack tip in the photograph was first identified by narrowing it down to a few pixels. This was then coupled with the discontinuity (or a *jump*) in displacement components across the crack faces was utilized to identify the crack tip. The possible error in locating the crack tip using this approach was approximately ±0.43 mm. In spite of this, locating a rapidly moving crack tip in a stiff composite producing relatively small deformation is quite demanding, particularly within a decorated speckle field, a notable disadvantage of DIC when compared to other optical methods such as moiré, CGS, and photoelasticity. Accordingly, a nonlinear analysis with the crack tip location as an unknown was implemented. That is, the coordinates of the crack tip as well as the two stress

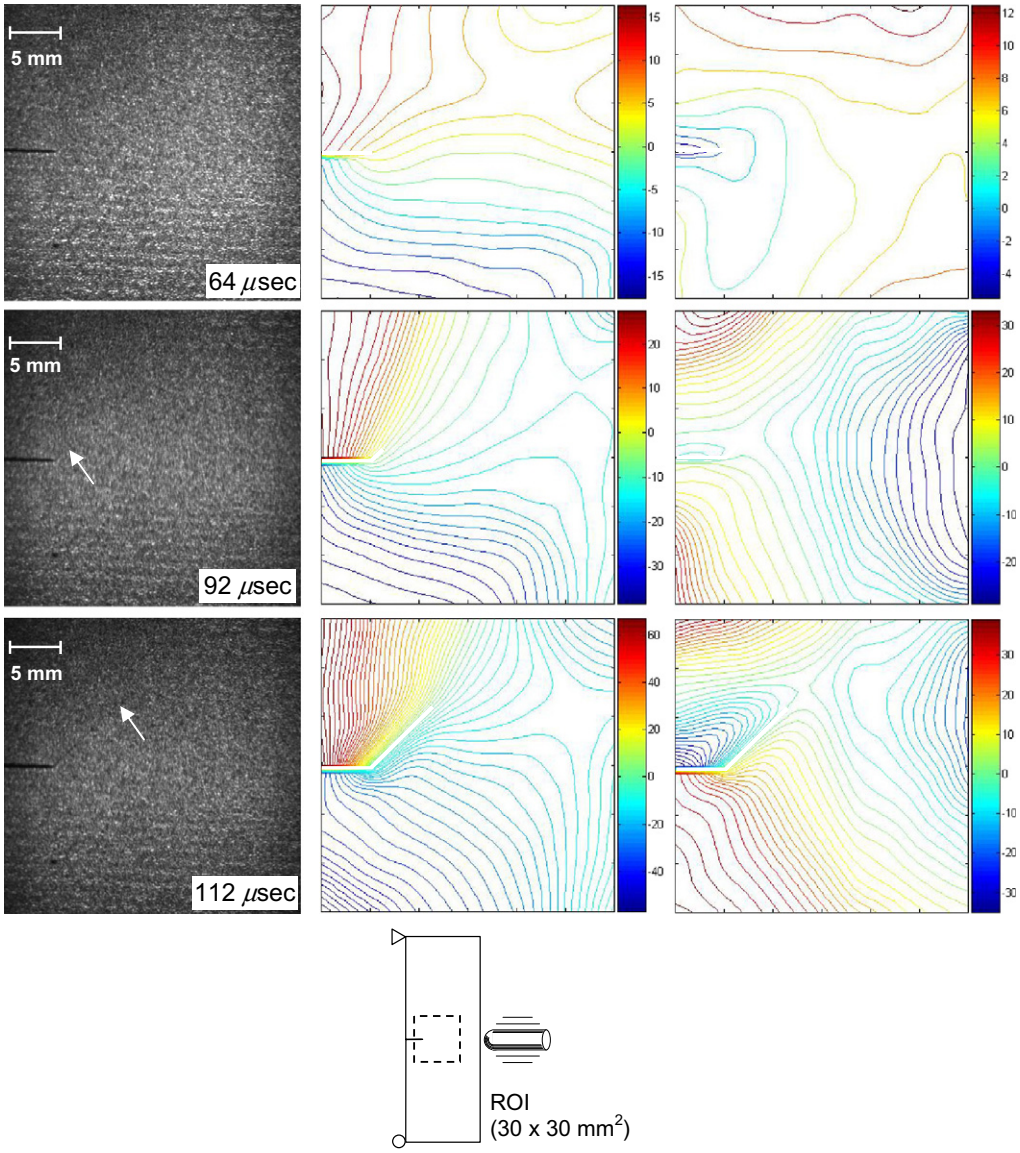

Fig. 7. Representative speckle images for dynamic case ($\beta = 45°$; 30×30 mm^2) with full-field opening (second column) and sliding (third column) displacement contours (crack initiation takes place at $t \sim 84$ μs): Moving crack tip is indicated by an arrow and the dark line is the initial crack in photographed images. Tick marks in the contour maps represent 5 mm intervals. Color-bars indicate displacement in micrometers. Contour interval here is 2 μm.

intensity factors were considered as unknowns in a set of nonlinear equations [44]. Yoneyama et al. [30] have successfully demonstrated such a scheme under quasi-static conditions for isotropic materials.

The nonlinear over-deterministic least-squares method was employed and the results are compared with the ones from using linear analysis in Fig. 11 for all four fiber orientation cases of dynamic loading. Until crack initiation the results from nonlinear analysis (NLSM) closely match those from the linear (LLSM) counterpart. However, in the post crack initiation regime, the stress intensity factor magnitudes show differences. Even though the two methods show similar trends for stress intensity factor histories, differences range from 10% to 30%. It should be emphasized that the largest difference between linear and nonlinear least-squares approach occurs for 0° fiber orientation and for the other fiber orientations the differences are less than 10%. Similar results were also observed for static cases but are not shown here for brevity. *In this work, results based on NLSM of displacement data are presented.*

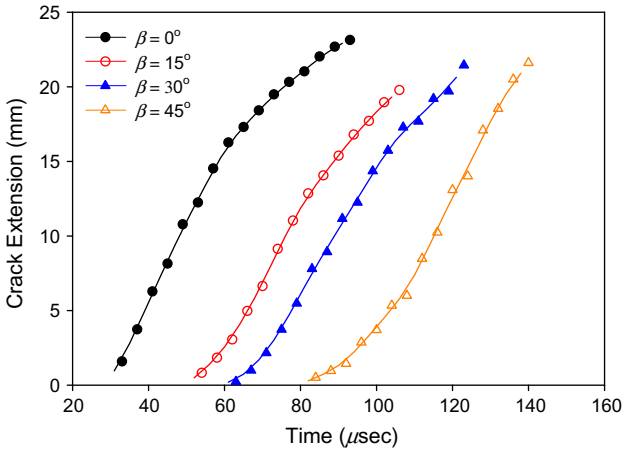

Fig. 8. Crack growth history for dynamic loading case. Initial slopes are approximately 510, 370, 310, 220 (m/s) for $\beta = 0°$, 15°, 30°, 45°, respectively.

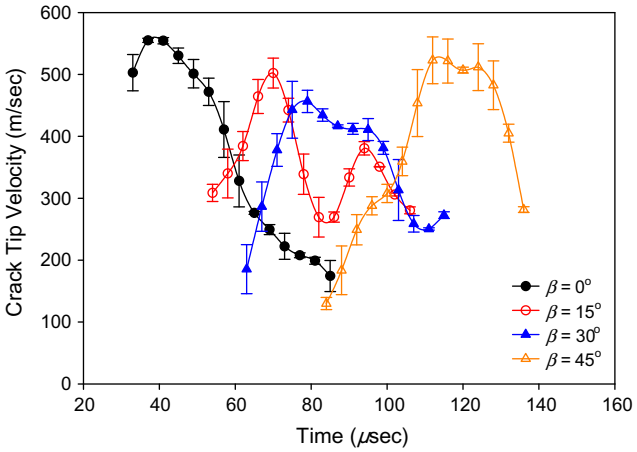

Fig. 9. Crack speed history for dynamic loading case for $\beta = 0°$, 15°, 30°, 45°.

It is also worth mentioning that an initial guess value of the current crack tip location is important for NLSM to be successful. In the computations, the convergence was declared when the difference between the nth and $(n+1)$th value was less than 0.01% of nth value. The benchmark tests suggested that any selection of initial value within a radius of one sub-image produced convergence in terms of fracture parameters. In this work, crack tip locations estimated as described earlier were fed as the initial guess values.

As noted earlier, although step-3 appears to be redundant, smoothing the displacement components from step-2 resulted in successful convergence of the least-squares algorithm and hence an improved result. In Fig. 12, the stress intensity factors extracted from displacements after each step of the three-step process are compared with one another for the case of $\beta = 0°$. All three steps show a stress intensity factor history that increases until crack initiation and decrease during growth. The SIF values estimated after step-1 are rather noisy with a significant oscillatory behavior. Those estimated after step-2 and -3, on the other hand, are relatively smooth and are close to each other.

5.2. Effect of fiber bridging

In fiber-reinforced composites, as a crack propagates, it leaves behind unbroken fibers bridging the newly formed crack flanks. The fiber bridges can be readily seen in Fig. 13. Due to these, the crack faces experience a closing force even as the crack front continues to propagate through the rest of the uncracked ligament along the fiber orientation direction. These closing forces counteract the crack driving forces, resulting in a reduction of crack tip stress intensification.

The samples under dynamic loading tend to be less prone to fiber bridging effects than the quasi-static counterparts. In the former, the two crack flanks were separated instantaneously (sample was broken into two at the end of the experiment) after crack initiation without having fibers bridging across them. The broken halves of the specimen also did not show significant fibers

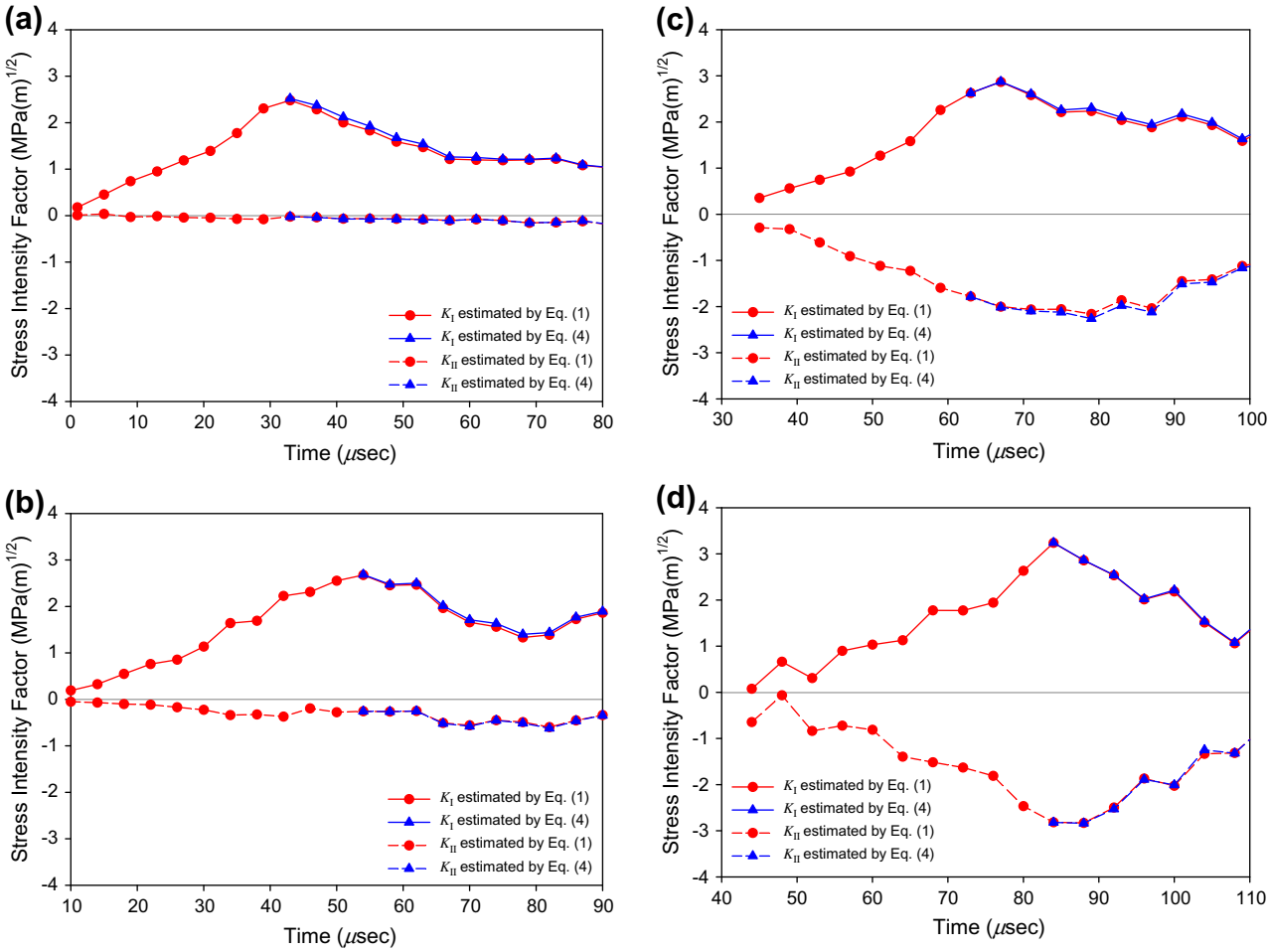

Fig. 10. Comparison of mode-I and -II stress intensity factors computed using quasi-static and dynamic governing equations: (a) $\beta = 0°$, (b) $\beta = 15°$, (c) $\beta = 30°$, (d) $\beta = 45°$.

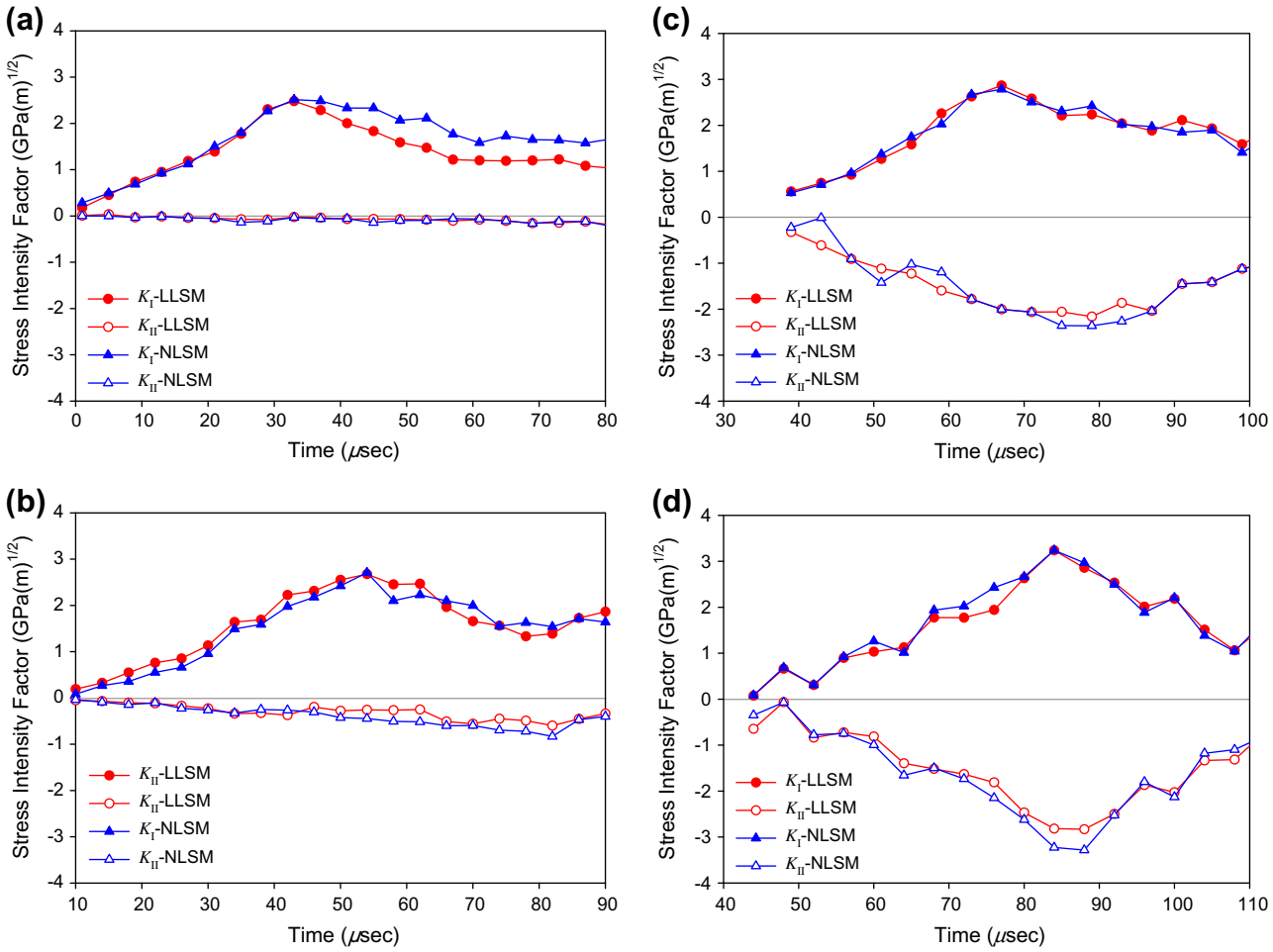

Fig. 11. Mode-I and -II stress intensity factors for dynamic cases estimated by linear least-squares method (LLSM) and nonlinear least-squares method (NLSM): (a) $\beta = 0°$, (b) $\beta = 15°$, (c) $\beta = 30°$, (d) $\beta = 45°$.

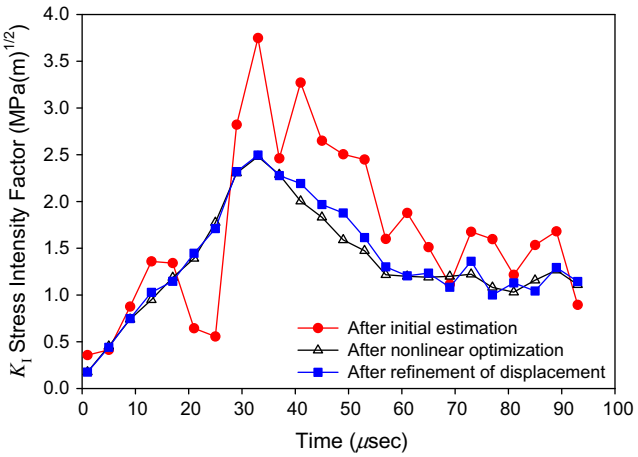

Fig. 12. Variation of stress intensity factors estimated from displacement fields obtained at various steps (steps 1–3) of DIC method.

pulled-out of the material bulk. On the other hand, in quasi-static cases, clumps of fibers (Fig. 13) continue to link the two crack faces even after the crack propagated over the entire sample width. That is, the two halves of the sample remained together at the end of experiments suggesting progressive failure of matrix and fiber–matrix interfaces during the fracture event.

5.3. Effects of fiber orientation angle

5.3.1. Quasi-static cases

The individual stress intensity factor histories for quasi-static cases are plotted in Fig. 14. The stress intensity factors at crack initiation (marked by arrows) increase with increasing fiber orientation angle. The mode-I and -II stress intensity factor histories (K_I and K_{II}) show that stress intensity factors monotonically increase up to crack initiation. Estimated errors of K_I and K_{II} are shown at a few selected points for legibility. These error bars were assessed based on crack tip location and the selection of data points in the crack tip vicinity in the least-squares analysis.[2] The K_{II} plots deviate from each other rather early in the loading history when compared to the ones for K_I. The magnitudes of K_{II} generally increase with increasing fiber orientation. In the initial stages of loading, there are noticeable oscillations in the K_I histories as the crack expectedly meanders along fibers and fiber–matrix interfaces. This is also partly due to imperfect alignment of fibers due to the composite fabrication process. In Fig. 14, it is noticeable that the maximum stress intensity factor does not occur at or near crack initiation (crack initiation points are indicated by an arrow). Even after the crack initiates, stress intensity factors continue to increase. This behavior is much more significant for higher fiber orientation angles and clearly indi-

[2] As mentioned earlier, data collected for least-squares analysis was generally in the angular range of −135° to 135°. Error bars were assessed based on data sets analyzed in the range of −150° to 150° and −120° to 120°.

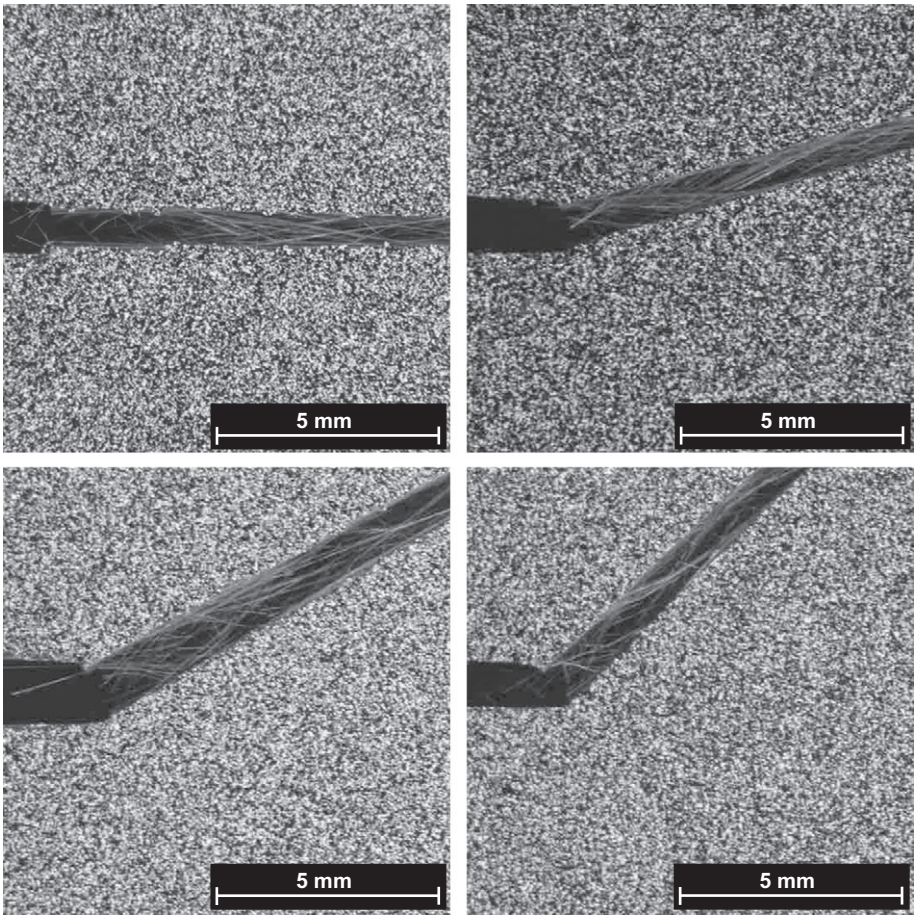

Fig. 13. Fibers bridges across crack flanks for 0°, 15°, 30°, and 45° (from left to right) fiber orientations in quasi-static experiments. Unit is in mm.

cates that the material experiences stable fracture under quasi-static loading conditions. Such a gradual failure could be explained from crack face bridging with fibers tending to close the two crack faces as seen in Fig. 13. The crack growth along paths dictated by non-zero K_{II} is also unique to fracture of composite samples. This is expected because the crack propagation path is restricted to weak fiber–matrix interfaces. Such a feature differentiates the fracture behavior of fiber-reinforced composites from those of isotropic materials. (The mixed-mode crack in an isotropic material is known to follow a path dictated by mode mixity approaching zero (or K_{II} becoming zero) just before crack initiation, indicating that crack initiation occurs under the dominant mode-I condition [35].) The subsequent crack path in isotropic materials also coincides with mode mixity of zero or K_{II} zero.

5.3.2. Dynamic cases

The variation of individual stress intensity factors as a function of time for all four fiber orientations are presented in Fig. 15. As in the quasi-static cases, the stress intensity factor at or near crack initiation increases with increasing β. As stated earlier, stress intensity factors monotonically increase prior to crack initiation and attain a peak value at crack initiation. However, the patterns such as the initial slope, location of the peak value and others seen in Fig. 15 are quite different when compared to the quasi-static counterparts. In each of the four cases, following crack initiation the mode-I stress intensity factors decrease monotonically. The magnitude of mode-II stress intensity factors, on the other hand, generally increases after crack initiation potentially due to fiber entanglement and/or crack face friction (in case of non-zero fiber orientation angles). Furthermore, as in the quasi-static cases, the non-zero K_{II} in the post crack initiation regime is unlike the ones for the isotropic materials where crack growth generally occurs along a path dictated by the $K_{II} = 0$ condition in the absence of weak planes.

5.4. Fracture toughness

The energy release rate (or crack driving force), which incorporates both K_I and K_{II}, for quasi-static and dynamic loading conditions is compared next. Due to uncertainty about the exact time instant of crack initiation, the average of three values, one immediately before *apparent* crack initiation, one at crack initiation, and one immediately after crack initiation, is used for quasi-static fracture toughness assessment. The energy release rate G is expressed as [8]

$$G = \frac{\eta}{2c_{66}R(v)}\sqrt{1-\left(\frac{1+\gamma}{\sqrt{\lambda}\eta^2\alpha_l+\alpha_s}\right)}\left(\alpha_l K_I^2+\sqrt{\lambda}\alpha_s K_{II}^2\right) \tag{7}$$

for a dynamically moving crack (after crack initiation) in an orthotropic medium. Eq. (7) can be reduced to

$$G = s_{11}\sqrt{\frac{1+\rho}{2}}\left(\frac{K_I^2}{\lambda^{3/4}}+\frac{K_{II}^2}{\lambda^{1/4}}\right) \tag{8}$$

for a dynamically loaded stationary crack (before crack initiation) in an orthotropic medium. Note that unlike Eq. (8), Eq. (7) is a function of the crack-tip velocity (v).

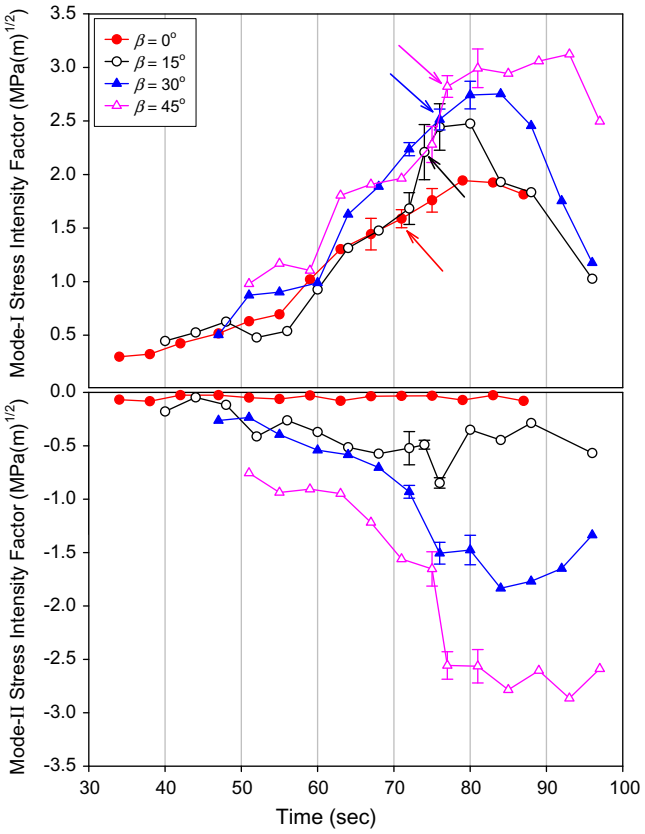

Fig. 14. Mode-I and -II stress intensity factor histories for various fiber orientation angles from quasi-static loading experiments. Crack initiation times are indicated by arrows.

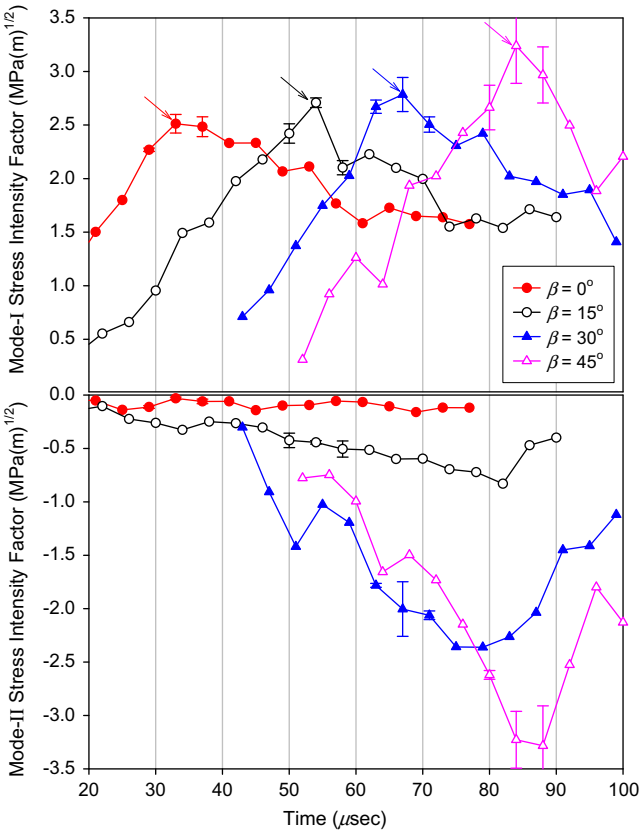

Fig. 15. Stress intensity factor histories for various fiber orientation angles under dynamic loading condition. Data points corresponding to crack initiation are indicated by arrows.

The energy release rate for an orthotropic medium under quasi-static loading condition is expressed in terms of stress intensity factors and compliance elements [38]:

$$G = \sqrt{\sqrt{\frac{S_{22}}{S_{11}}} + \frac{2S_{12} + S_{66}}{2S_{11}}} \left(\sqrt{\frac{S_{11}S_{22}}{2}} K_{\mathrm{I}}^2 + \frac{S_{11}}{\sqrt{2}} K_{\mathrm{II}}^2 \right) \tag{9}$$

assuming K_{I} and K_{II} to be uncoupled.

The dynamic crack driving force histories are shown in Fig. 16 along with the quasi-static ones. In each case, the crack driving force increases monotonically up to crack initiation. There are, however, differences in fracture toughness (critical crack driving force) values at initiation (marked by the shaded strips), between static and dynamic cases. Generally, the dynamic crack driving force values at initiation are 1.2–2.5 times the static counterparts with the largest corresponding to the 0° fiber orientation. The other fiber orientations, 15°, 30° and 45°, all have a similar increase in dynamic values relative to quasi-static counterparts in the range of 1.2–1.4. Following crack initiation, in each case, the crack driving force first rapidly decreases and then attains a nearly constant value. Interestingly, the attained constant value in the 0° case is ~1.0 (or dynamic value attains the static counterpart) beyond ~60 μs, after which the crack-velocity becomes less than 200 m/s, as in Fig. 9a, implying a crack propagates as if it is under static loading condition. A similar observation was made for a different graphite/epoxy system (IM7/8551–7) by Liu et al. [8], in which fracture toughness reached a peak value at initiation, and dropped immediately, and attained a constant value close to that of the static value. For 15°, 30° and 45° fiber orientations, however, the crack attains constant values of approximately 60%, 40% and 20% of the quasi-static counterpart in the window of observation. Interestingly, the corresponding absolute value of fracture toughness translates into a value 0.21 ± 0.02 kN/m in each of the fiber orientations and could be likely viewed as an arrest fracture toughness of unidirectional T800/3900-2 graphite/epoxy material.

It is important to note that magnitudes presented in Fig. 14 are based on quasi-static values of elastic constants for T800/3900-2 graphite/epoxy composite. It is likely that elastic constants of a graphite/epoxy system are different at higher strain rates. Daniel et al. [2] reported that E_1, G_{12}, and ν_{12} increase but only modestly in a strain rate range of 10^{-5}–10^{2} s^{-1}. In the same range, E_2 (modulus in the matrix dominant direction) is shown to increase more significantly. If it is assumed that the material in the current work has a behavior similar to the composite system studied in Ref. [2], the dynamic stress intensity factors and the crack driving forces computed from those elastic constants at higher strain rate are expected to be higher than the ones shown in Fig. 14 and in Fig. 16.

Lastly, it is instructive to compare fracture toughness at initiation for all cases. The fracture toughness at crack initiation in composites increases with increasing fiber orientation angle. For the particular graphite/epoxy used in the present work such a behavior can be quantified and is shown in Fig. 17. In this case, the fracture toughness is plotted as a function of E_{xx}-to-E_{yy} ratio, the degree-of-anisotropy. The fracture toughness decays with increasing degree-of-anisotropy. Interestingly, the values corresponding to dynamic fracture are consistently higher than the quasi-static ones. Parhizgar et al. [45] reported a similar result based on their CT specimens made of a glass fiber/epoxy system for quasi-static loading. Furthermore, the variation of dynamic fracture toughness is nearly an exponential decay with a modest increase in the degree-of-anisotropy. The quasi-static values on the other hand show a more gradual variation. A relatively dominant crack bridging observed

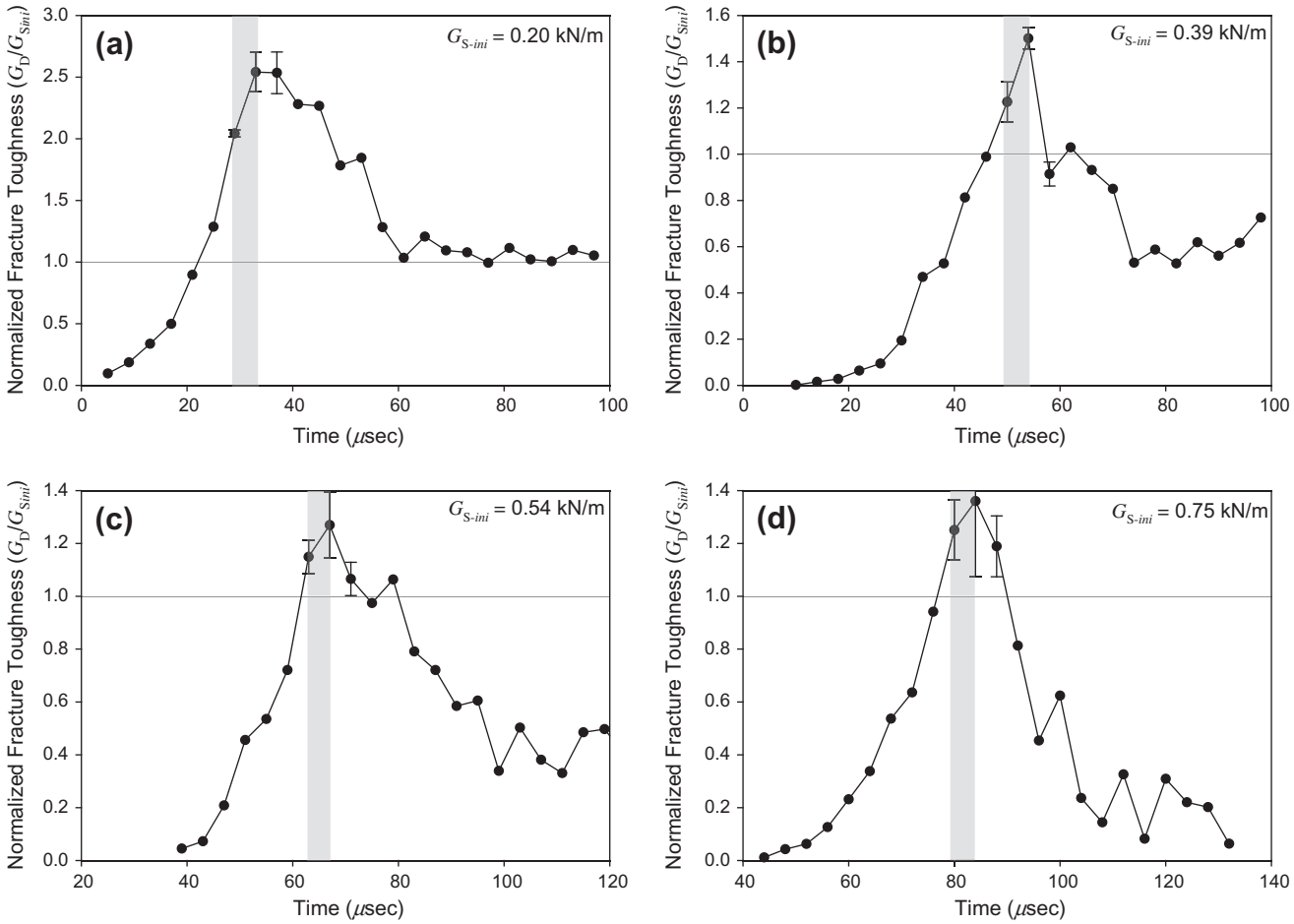

Fig. 16. Dynamic fracture toughness histories compared with quasi-static values at crack initiation: (a) $\beta = 0°$, (b) $\beta = 15°$, (c) $\beta = 30°$, (d) $\beta = 45°$. Values presented here are normalized by static fracture toughness at initiation, $G_{S\text{-}ini}$. Uncertainty in determining crack initiation time is represented by the shaded strip.

under quasi-static loading conditions is likely responsible for this difference.

6. Conclusions

In this work, loading-rate effects on fracture behavior of unidirectional T800/3900-2 graphite/epoxy composite panels are studied. Composite samples with edge cracks are subjected to quasi-static and impact loading in symmetric loading configurations. The fiber orientation angle is varied relative to the crack (and impact loading) direction in order to produce mixed-mode fracture. The method of 2D digital image correlation along with high-speed digital photography is used to record growth histories and in-plane displacements in the crack tip vicinity under dynamic conditions. The crack length history is used to estimate instantaneous crack velocities for different fiber orientations. The uncertainty of knowing the current crack tip position among the decorated speckles is addressed by carrying out nonlinear and linear over-deterministic least-squares analyses on displacement fields to extract mode-I and -II stress intensity factors and energy release rates. The differences in results between the two methods are in the range of 10–30% with the highest difference in mode-I configuration with 0° fiber orientation. The fracture parameters obtained from quasi-static and dynamic experiments for various different fiber orientation angles are also compared.

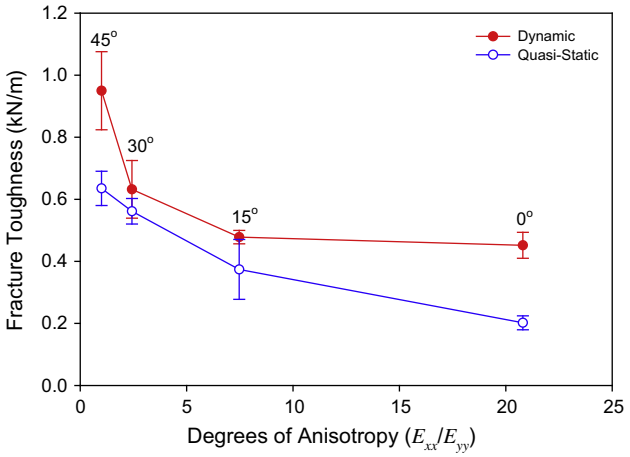

Fig. 17. Variation of energy release rate (G) as a function of degree-of-anisotropy (E_{xx}/E_{yy}) of the composite.

The fracture behavior is loading rate sensitive. Based on fracture surface morphology, under quasi-static loading conditions the crack faces are bridged by unbroken fibers resulting in the two halves of a fractured sample held together even after the crack front passes a location on the uncracked ligament. In the dynamic cases, on the other hand, there are no detectable fiber bridges with samples spontaneously broken into two during experiments.

For both static and dynamic cases, the stress intensity factor at or near crack initiation increases with increasing fiber orientation angle. Furthermore, stress intensity factor monotonically increases prior to crack initiation and has a peak value at or near crack initi-

ation. The post crack initiation behaviors show differences in terms of fracture parameters. In dynamic cases, the post-initiation stress intensity factors drop rapidly whereas the quasi-static counterparts show a modest increase. Interestingly for both cases, mode mixity in the post-initiation period is different but nearly stationary for each fiber orientation. This is attributed to the weak fiber direction present in unidirectional composites. The crack driving force for a dynamically growing mode-I crack (0° fiber orientation) attains the value of the quasi-static counterpart soon after crack initiation. In case of non-zero fiber orientations, however, dynamically growing cracks reach a fraction of the corresponding quasi-static crack initiation value. At crack initiation, the crack driving force of a dynamic crack, regardless of the fiber orientation angle, is higher than its static counterpart.

Acknowledgements

This research was sponsored by the NASA-LaRC under Cooperative Agreement Number NNX07AC64A.

References

[1] Gilat A, Goldberg RK, Roberts GD. Experimental study of strain-rate-dependent behavior of carbon/epoxy composite. Compos Sci Technol 2002;62(10–11):1469–76.
[2] Daniel IM, Hamilton WG, LaBedz RH. Strain rate characterization of unidirectional graphite/epoxy composite. In: Daniel IM, editor. Composite materials: testing and design, ASTM STP 787. Philadelphia: American Society for Testing and Materials; 1982. p. 393–413.
[3] Gillespie JW, Carlsson LA, Smiley AJ. Rate-dependent mode-I interlaminar crack growth mechanisms in graphite/epoxy and graphite/peek. Compos Sci Technol 1987;28(1):1–15.
[4] You H, Yum YJ. Loading rate effect on mode I interlaminar fracture of carbon/epoxy composite. J Reinf Plast Compos 1997;16(6):537–49.
[5] Smiley AJ, Pipes RB. Rate effects on mode I interlaminar fracture toughness in composite materials. J Compos Mater 1987;21(7):670–87.
[6] Tirosh J. The mixed mode fracture of unidirectional fibrous composites. Eng Fract Mech 1980;13(1):119–27.
[7] Donaldson SL. Fracture toughness testing of graphite/epoxy and graphite/peek composites. Composites 1985;16(2):103–12.
[8] Liu C, Rosakis AJ, Stout MG. Dynamic fracture toughness of a unidirectional graphite/epoxy composite. In: Am soc mech eng appl mech div AMD (ASME-IMECE 2001). Dynamic failure in composite materials and structures, vol. 247; 2001. p. 1–12.
[9] Shukla A, Agarwal BD, Bhushan B. Determination of stress intensity factor in orthotropic composite materials using strain gages. Eng Fract Mech 1989;32(3):469–77.
[10] Khanna SK, Shukla A. Development of stress field equations and determination of stress intensity factor during dynamic fracture of orthotropic composite materials. Eng Fract Mech 1994;47(3):345–59.
[11] Khanna SK, Shukla A. On the use of strain gages in dynamic fracture mechanics. Eng Fract Mech 1995;51(6):933–48.
[12] Rosakis AJ. Analysis of the optical method of caustics for dynamic crack propagation. Eng Fract Mech 1980;13(2):331–47.
[13] Kobayashi T, Dally JW. Dynamic photoelastic determination of the $\dot{a}$—K relation for 4340 alloy steel. In: Erdogan F, editor. Fracture mechanics, ASTM STP 711. Philadelphia: American Society for Testing and Materials; 1980. p. 189–210.
[14] Kokaly MT, Lee J, Kobayashi AS. Moire interferometry for dynamic fracture study. Opt Lasers Eng 2003;40(4):231–47.
[15] Lin ST, Feng Z, Rowlands RE. Thermoelastic determination of stress intensity factors in orthotropic composites using the J-integral. Eng Fract Mech 1997;56(4):579–92.
[16] Yao XF, Xu W, Jin GC, Yeh HY. Low velocity impact study of laminate composites with mode I crack using dynamic optical caustics. J Reinf Plast Compos 2004;23(17):1833–44.
[17] Tippur HV. Coherent gradient sensing: a Fourier optic analysis and applications to fracture. Appl Opt 1992;31(22):4428–38.
[18] Tippur HV, Rosakis AJ. Quasi-static and dynamic crack growth along biomaterial interfaces: a note on crack tip field measurements using coherent gradient sensing. Exp Mech 1991;31(3):243–51.
[19] Lambros J, Rosakis AJ. Dynamic crack initiation and growth in thick unidirectional graphite/epoxy plates. Compos Sci Technol 1997;57(1):55–65.
[20] Huang Y, Wang W, Liu C, Rosakis AJ. Analysis of intersonic crack growth in unidirectional fiber-reinforced composites. J Mech Phys Solids 1999;47(9):1893–916.
[21] Coker D, Rosakis AJ. Experimental observations of intersonic crack growth in asymmetrically loaded unidirectional composite plates. Philos Mag A Phys Condens Matter Struct Defects Mech Prop 2001;81(3):571–95.
[22] McNeill SR, Peters WH, Sutton MA. Estimation of stress intensity factor by digital image correlation. Eng Fract Mech 1987;28(1):101–12.
[23] Bruck HA, McNeill SR, Sutton MA, Peters III WH. Digital image correlation using Newton–Raphson method of partial differential correction. Exp Mech 1989;29(3):261–7.
[24] Tan H, Liu C, Huang Y, Geubelle PH. The cohesive law for the particle/matrix interfaces in high explosives. J Mech Phys Solids 2005;53(8):1892–917.
[25] Hild F, Périé JN, Lamon J, Puyo-Pain M. On the use of digital image correlation to analyze the mechanical properties of brittle matrix composites. Ceram Trans 2006;175:63–76.
[26] Abanto-Bueno J, Lambros J. An experimental study of mixed mode crack initiation and growth in functionally graded materials. Exp Mech 2006;46(2):179–96.
[27] Mekky W, Nicholson PS. The fracture toughness of Ni/Al_2O_3 laminates by digital image correlation I: experimental crack opening displacement and R-curves. Eng Fract Mech 2006;73(5):571–82.
[28] Han J, Siegmund T. A combined experimental–numerical investigation of crack growth in a carbon–carbon composite. Fatigue Fract Eng Mater Struct 2006;29(8):632–45.
[29] Dawicke DS, Sutton MS. CTOA and crack-tunneling measurements in thin sheet 2024–t3 aluminum alloy. Exp Mech 1994;34(4):357–68.
[30] Yoneyama S, Morimoto Y, Takashi M. Automatic evaluation of mixed-mode stress intensity factors utilizing digital image correlation. Strain 2006;42(1):21–9.
[31] Abanto-Bueno J, Lambros J. Investigation of crack growth in functionally graded materials using digital image correlation. Eng Fract Mech 2002;69(14–16):1695–711.
[32] Rethore J, Gravouil A, Morestin F, Combescure A. Estimation of mixed-mode stress intensity factors using digital image correlation and an interaction integral. Int J Fract 2005;132(1):65–79.
[33] Rethore J, Roux S, Hild F. Noise-robust stress intensity factor determination from kinematic field measurements. Eng Fract Mech 2008;75(13):3763–81.
[34] Mogadpalli GP, Parameswaran V. Determination of stress intensity factor for cracks in orthotropic composite materials using digital image correlation. Strain 2008;44(6):446–52.
[35] Kirugulige MS, Tippur HV, Denney TS. Measurement of transient deformations using digital image correlation method and high-speed photography. Appl Opt 2007;46(24):5083–96.
[36] Kirugulige MS, Tippur HV. Measurement of fracture parameters for a mixed-mode crack driven by stress waves using image correlation technique and high-speed digital photography. Strain 2009;45(2):108–22.
[37] Lee D, Tippur HV, Kirugulige MS, Bogert P. Experimental study of dynamic crack growth in unidirectional graphite/epoxy composite using digital image correlation method and high-speed photography. J Compos Mater 2008;43(19):2081–108.
[38] Sih GC, Paris PC, Irwin GR. On cracks in rectilinearly anisotropic bodies. Int J Fract Mech 1965;1:189–203.
[39] Stroh AN. Dislocations and cracks in anisotropic elasticity. Philos Mag 1958;3:645–6.
[40] Xia KW, Chalivendra VB, Rosakis AJ. Observing ideal 'self-similar' crack growth in experiments. Eng Fract Mech 2006;73(18):2748–55.
[41] Chen DJ, Chiang FP, Tan YS, Don HS. Digital speckle-displacement measurement using a complex spectrum method. Appl Opt 1993;32(11):1839–49.
[42] Morozov VA. Regularization methods for ill-posed problems. Ann Arbor (Michigan): CRC Press; 1993.
[43] Reinsch CH. Smoothing by spline functions. Numer Math 1967;10:177–83.
[44] Sanford RJ. Application of the least-squares method to photoelastic analysis. Exp Mech 1980;20(6):192–7.
[45] Parhizgar S, Zachary LW, Sun CT. Determination of fracture toughness of unidirectionally fiber-reinforced composites. In: Fracture of composite materials. Proceedings of the 2nd USA–USSR symposium; 1982. p. 215–30.